

Fracture Toughness and *R*-Curve Behavior of Laminated Brittle-Matrix Composites

D.R. BLOYER, K.T. VENKATESWARA RAO and R.O. RITCHIE

The fracture toughness and resistance-curve behavior of relatively coarse-scale, niobium/niobium aluminide (Nb/Nb₃Al) laminated composites have been examined and compared to other Nb/Nb₃Al composites with (*in situ*) Nb particulate or microlaminate reinforcements. The addition of high aspect-ratio Nb reinforcements, in the form of 20 vol. pct of 50- to 250- μ m-thick layers, was seen to improve the toughness of the Nb₃Al intermetallic matrix by well over an order of magnitude, with the toughness increasing with Nb layer thickness. The orientation of the laminate had a small effect on crack-growth resistance with optimal properties being found in the crack arrester, as compared to the crack divider, orientation. The high fracture toughness of these laminates was primarily attributed to large (~1- to 6-mm) crack-bridging zones formed by intact Nb layers in the crack wake; these zones were of sufficient size that large-scale bridging (LSB) conditions generally prevailed in the samples tested. Resistance-curve modeling using weight function methods permitted the determination of simple approximations for the bridging tractions, which were then used to make small-scale bridging (SSB) predictions for the steady-state toughness of each laminate.

I. INTRODUCTION

IN recent years, several intermetallic compounds have been developed with many desirable properties for potential use in structural and aerospace applications;^[1] these properties include high melting points (typically ~1500°C to 2000°C), low densities (typically 4 to 8 g/cm³), and good creep resistance.^[2-5] However, the disadvantage of these materials is that they are often very brittle due to a high resistance to dislocation motion resulting from their relatively complex, ordered crystal structures. For example, in comparison to toughnesses of ~50 to 100 MPa \sqrt{m} shown by traditional Ti- and Ni-based alloys, intermetallics such as Nb₃Al and MoSi₂ typically display fracture toughness, K_{IC} , values below ~4 MPa \sqrt{m} ; in fact, even in the more “ductile” compounds such as γ -TiAl, intrinsic toughnesses are typically ~10 MPa \sqrt{m} .

To improve the low intrinsic toughnesses of intermetallics, extrinsic toughening techniques that invoke crack-tip shielding mechanisms are often used in alloy and microstructural development. Such mechanisms, which include crack bridging *via* ductile or brittle reinforcements, primarily act behind the crack tip and locally screen the crack from the applied (far-field) driving force.^[6,7] Using ductile reinforcements, the principle is to promote crack-particle interactions to create bridging ligaments in the crack wake, which deform plastically and impart closing tractions on the crack faces.

Under small-scale bridging (SSB) conditions,* the in-

*Small-scale bridging conditions apply where the bridging tractions act over a distance that is small relative to the crack length and in-plane specimen dimensions; in this regime, G_b is independent of crack length and specimen geometry. With larger bridging zones, the traction contribution is a function of crack length and geometry; this is referred to as large-scale bridging (LSB).

crease in fracture energy due to ductile reinforcements, G_b , can be formulated in terms of the physical properties of the reinforcement and interface by relating it to a nondimensional work of rupture, χ :^[8,9,10]

$$\chi = \int_0^{u^*/r} \frac{\sigma(u/r)}{\sigma_0} \cdot d(u/r) \quad [1]$$

where $\sigma(u)$ is the stress-displacement function of the bridging tractions; u^* is the displacement at failure of the bridging ligament; and σ_0 and r are, respectively, the flow stress and characteristic dimension of the reinforcement, such that^[8]

$$G_b = f \cdot r \cdot \sigma_0 \cdot \chi \quad [2]$$

where f is the volume fraction of reinforcement intercepted by the crack. This additional energy to fracture the bridging ligaments is typically exhibited in the form of resistance-curve (*R*-curve) behavior, where the (crack-growth) toughness increases with crack extension, commensurate with the development of a bridging zone in the crack wake.

Alternatively, the toughening can be described in terms of stress intensities, where the steady-state toughness, K_{SS} , can be modeled by superposing (using G and then converting back to K) the reinforcement toughening contribution with the intrinsic fracture toughness of the composite, K_0 (*i.e.*, the matrix or crack-initiation toughness*):^[8,9,10]

*The crack-initiation toughness of the composite can be markedly higher than the matrix toughness, for example, where the crack must renucleate across a second phase.^[30,33]

$$K_{SS} = \sqrt{K_0^2 + E'f\sigma_0r\chi} \quad [3]$$

D.R. BLOYER, Postdoctoral Researcher, and R.O. RITCHIE, Professor, are with the Department of Materials Science and Mineral Engineering, University of California, and the Materials Sciences Division, Lawrence Berkeley National Laboratory, Berkeley, CA 94720-1760. K.T. VENKATESWARA RAO, formerly Research Engineer with the Department of Materials Science and Mineral Engineering, University of California, is Manager of R&D, Vascular Intervention Group, Guidant Corporation, Santa Clara, CA 95052.

Manuscript submitted December 9, 1997.

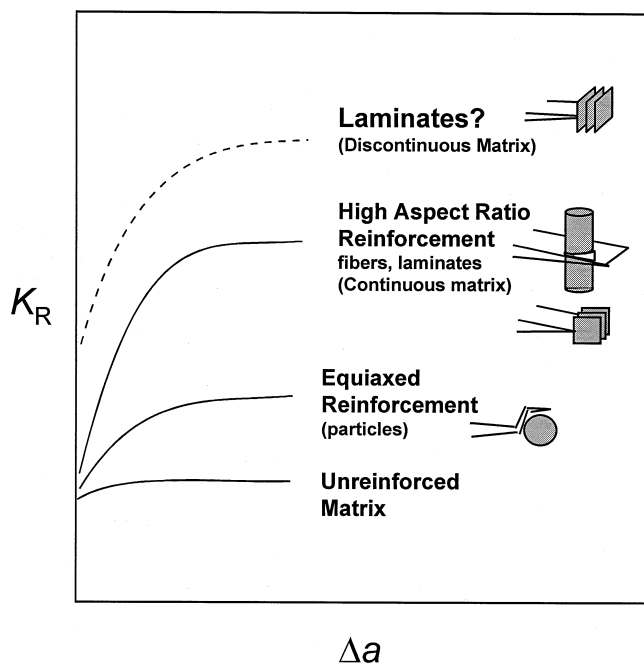


Fig. 1—Schematic of achievable trends in toughness for various composite reinforcement geometries.

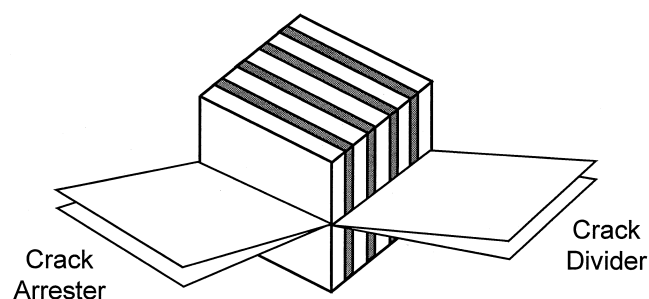


Fig. 2—Laminate composite orientation.

where E' is the plane-strain composite modulus (assuming a Poisson's ratio of 0.3).

The degree of composite toughening is a marked function of the reinforcement morphology, properties, and its interface with the matrix. Numerous reinforcement shapes have been employed in various ductile/brittle composite systems, including particulates^[11–16] and fibers;^[8,17–21] laminate reinforcements, however, often show the best fracture resistance, as illustrated schematically in Figure 1.^[8,22–42] The advantage of laminate reinforcements is that the high aspect ratio of the second phase increases the probability of intersection with the crack, thereby enhancing R -curve (*i.e.*, crack-growth) toughening by creating a larger shielding zone of continuous bridges in the crack wake. In addition, for the arrester orientations, the initiation toughness may also be enhanced because the crack has to renucleate across the reinforcing layer. Nevertheless, the effect of the scale of the ductile reinforcement in layered microstructures is not completely clear. Finer microlayered structures are typically favored to enhance composite strength, whereas (from Eq. [2]) coarser macrolayered structures are expected to show the best fracture resistance.

In the present study, we examine the toughness and R -curve behavior in a model system, specifically a Nb-reinforced Nb₃Al composite, where toughening is achieved by the addition of 20 vol. pct of ductile Nb layers having layer dimensions in the tens to hundreds of microns. Results are compared with prior studies on Nb/Nb₃Al composites with the Nb as $\sim 20 \mu\text{m}$ particulate formed *in situ* by powder-metallurgy processing,^[15,16] or as 2- μm -thick (magnetron sputtered) layers to form a microlaminate.^[35,36,39]

II. EXPERIMENTAL PROCEDURES

A. Laminate Processing

The Nb-reinforced Nb₃Al laminates were processed in two orientations: the “crack arrester” (0 deg or C-L), where the crack grows perpendicular to, yet sequentially through, the layers; and the “crack divider” (C-R), where the crack plane is normal to the plane of layers, but the crack advances through all the layers simultaneously (Figure 2). To investigate the effect of laminate thickness, materials with three different Nb layer thicknesses were prepared while maintaining a constant volume fraction of a nominal 20 vol. pct Nb in each case. The respective thicknesses were as follows:

- (1) 50- μm Nb/200- μm Nb₃Al,
- (2) 125- μm Nb/500- μm Nb₃Al, and
- (3) 250- μm Nb/1000- μm Nb₃Al.

Nb₃Al powder was prepared by reaction synthesis of elemental Nb (CERAC,* 99.8 pct, -325 mesh for 125- and

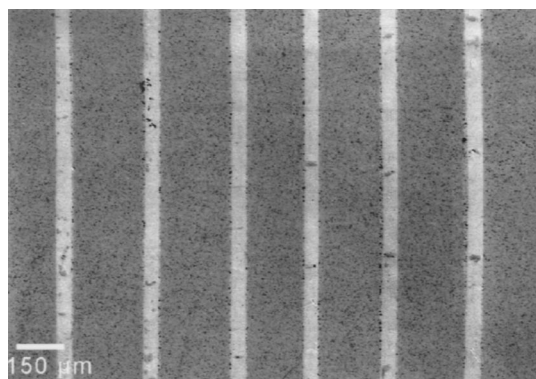
*CERAC is a trademark of Cerac, Inc., Milwaukee, WI.

250- μm Nb laminates, and CERAC, 99.8 pct, 5 μm or less for the 50- μm Nb laminates) and Al (Valimet, 99.3 pct, -325 mesh) powders in the molar ratio of 0.76Nb-0.24Al. These were mixed in a ball mill for approximately 0.5 hours and then heated in a helium atmosphere at 1400 °C for 4 hours to form Nb₃Al. The reacted powder was subsequently ball milled for approximately 0.5 hours, reheated to 1400 °C for an additional 4 hours to complete the reaction, and then ball milled again for 1 hour to reduce any agglomerated particles prior to use in composite fabrication.

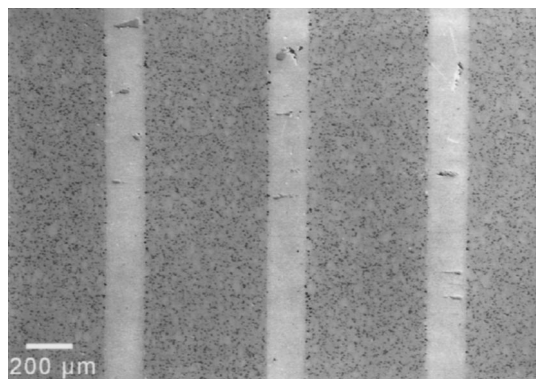
The laminates were prepared by sequentially cold pressing layers of the Nb₃Al powder between the Nb foils (Rembar Co., Dobbs Ferry, N.Y. and Alfa Aesar Co., trademark of Johnson Matthey Co., Ward Hill, MA) in a graphite mold and then hot pressing in an argon atmosphere to create composite cylinders or discs. The 50- μm Nb laminates were pressed at 1500 °C for 25 minutes under 37 MPa of pressure, and the 125- and 250- μm Nb laminates were pressed at 1650 °C for 25 minutes under 37 MPa of pressure, with the exception of the 125- μm Nb arrester specimens, which were pressed at 1680 °C for 40 minutes.* The resulting microstructures of the laminates consisted of

*For the 125- μm Nb laminate, this resulted in a slightly smaller effective volume fraction of Nb reinforcement in the arrester, compared to the divider, orientation.

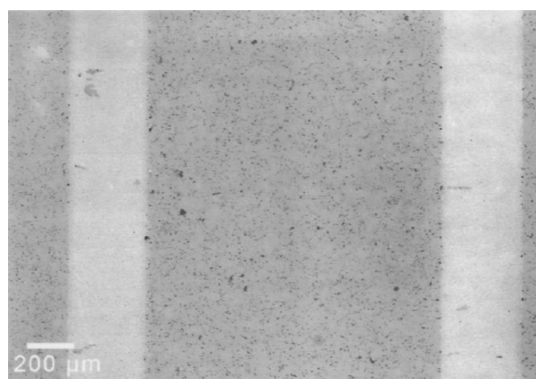
evenly spaced, parallel layers of Nb₃Al intermetallic separated by layers of Nb metal (Figure 3).



(a)



(b)



(c)

Fig. 3—Micrographs of the composite microstructures for the (a) 50- μm Nb/200- μm Nb₃Al laminate, (b) 125- μm Nb/500- μm Nb₃Al laminate, and (c) 250- μm Nb/1000- μm Nb₃Al laminate.

Table I. Effective Reinforcement Thickness and Volume Fraction

Nominal Nb Thickness (μm)	Effective Nb Thickness (μm)	Effective Nb Volume Fraction
50	40 (40)*	0.16 (0.16)
125	85 (95)	0.14 (0.15)
250	218 (218)	0.17 (0.17)

*Numbers in parentheses represent divider specimens.

B. Microstructural Evaluation

The grain sizes of the metallic and intermetallic layers were determined by metallographically etching polished

specimens using a standard Nb etch taken from the 1992 ASTM Standard E407 (etch no. 164). The average Nb₃Al grain sizes, estimated using a simple line-intercept method, were ~ 4 and $10 \mu\text{m}$ for the laminates processed at 1500°C and 1650°C to 1680°C , respectively. Corresponding grain sizes in the Nb were ~ 100 , 220 , and $300 \mu\text{m}$ for the 50-, 125-, and 250- μm -thick Nb layers, respectively. During processing, the Nb grains grew in such a manner that they encompassed the entire thickness of the metal layer, but there were many grains along the length of the layer. As a result, the grain sizes were measured as a “linear” grain size along the length of the metal layer, and the grain thickness was that of the Nb reinforcing layer.

X-ray line scans indicated there was some diffusion of aluminum into the Nb reinforcing layers, which created a diffusion layer between the metal and intermetallic. The presence of the reaction layer was considered to reduce the effective thickness of the Nb layer and increase the thickness of the matrix layer; this, in turn, resulted in slight differences in the effective volume fractions of reinforcement for the different laminates. Table I lists the effective Nb layer thickness and volume fraction measurements for the laminates prepared in this study.

C. Mechanical Testing

Single-edged notched bend beams, SE(B), with a loading span of 35 to 40 mm, were used to study the *R*-curve behavior of all the arrester laminates. The specimens had a thickness of $B = 3.5$ mm and a width of $W = 9.3$ mm in the 50- μm Nb/200- μm Nb₃Al laminates. Corresponding specimen sizes in the 125- μm Nb/500- μm Nb₃Al laminates were $B = 3.5$ mm and $W = 12.5$ mm and $B = 3.6$ mm and $W = 13.3$ mm for the 250- μm Nb/1000- μm Nb₃Al laminates.

Divider laminates, conversely, were assessed using 33-mm-wide, disc-shaped compact-tension, DC(T), specimens. Sample thicknesses were 2.8 mm in the 50- μm Nb/200- μm Nb₃Al laminates and 3.5 to 3.6 mm in the other two microstructures.

Prior to testing, all specimens were fatigue precracked to a crack length to width ratio, a/W , of at least 0.3. Precracking was conducted on servohydraulic testing machines at near-threshold stress-intensity ranges (with a load ratio of 0.1) in order to minimize microstructural damage ahead of the crack tip. The objective was to obtain a sharp crack, yet at the same time to minimize any bridging zones that may form in the crack wake prior to *R*-curve testing. *R*-curve testing was performed under manual displacement control at a displacement rate of 5 to 10 $\mu\text{m}/\text{min}$, with crack lengths monitored *in situ* using compliance and, principally, optical techniques. The data presented represent typical results from at least two samples.

III. RESULTS AND DISCUSSION

A. Fracture Toughness and *R*-Curve Behavior

1. Divider orientation

The *R*-curve results, plotted in Figure 4(a) for the divider orientation, illustrate that the addition of high aspect-ratio

ductile reinforcements leads to significant improvements in the fracture behavior of Nb_3Al . Compared with the fracture toughness of only $\sim 1 \text{ MPa}\sqrt{\text{m}}$ for monolithic Nb_3Al , the addition of 20 vol. pct of 50- μm -thick Nb layers resulted in an initiation toughness of $4.8 \text{ MPa}\sqrt{\text{m}}$ and a maximum toughness (on the R -curve) exceeding $10 \text{ MPa}\sqrt{\text{m}}$. The 125- and 250- μm Nb laminates yielded even better properties having initiation toughnesses of 6.7 and $7.1 \text{ MPa}\sqrt{\text{m}}$, respectively, and corresponding maximum toughnesses of about 15 and $20 \text{ MPa}\sqrt{\text{m}}$.

It should be noted that the present laminates contain only 20 vol. pct Nb (nominal), yet they exhibit markedly higher toughness than Nb particulate-toughened Nb_3Al composites, which contained twice the volume fraction of Nb^[16] (Figure 4(b)). Moreover, they displayed superior crack-growth toughness to microlaminates that consisted of 50 vol. pct of $\sim 2\text{-}\mu\text{m}$ -thick Nb layers in Nb_3Al .^[35,36,39] Specifically, crack extension occurred only over the first 200 μm of growth in the microlaminates, compared to stable cracking over several millimeters of crack extension in the present laminates. It is clear that with coarser ductile-phase layers, the brittle matrices require far less reinforcement to achieve significantly improved toughness properties; indeed, compared to particulate or microlaminate composites, the crack-initiation toughness, the maximum toughness, and the extent of subcritical crack growth prior to unstable fracture are all progressively enhanced with the coarser-scale layered reinforcements.

In the divider orientation, cracks were seen to tunnel ahead in the Nb_3Al matrix, leaving extensive Nb bridging zones behind the crack tip to shield the far-field applied stress intensity. The order of magnitude increase in toughness over monolithic Nb_3Al shown by the present laminates was primarily attributed to this crack tunneling behavior.

It was anticipated that crack-initiation toughness values in the divider orientation would be equivalent to that of the intermetallic matrix; however, this behavior was not observed. It is believed that fatigue precracking virtually eliminates intact ductile second phase in the crack wake in most ductile-phase toughened materials;^[27] however, metallographic observations in the present study indicated that the crack tunneled forward between the layers and resulted in small bridging zones even during fatigue loading (Figure 5(a)). Consequently, it would appear that the measured initiation toughnesses in the crack-divider orientation are somewhat artificially elevated due to residual crack bridging resulting from precracking.

2. Arrestor orientation

Corresponding R -curves for the crack-arrestor orientation are shown in Figure 6. Consistent with previous investigations,^[30,33] the initiation toughness, K_0 , was seen to increase with increasing layer thickness, giving values of 7.3, 9, and $10.4 \text{ MPa}\sqrt{\text{m}}$ for the 50-, 125- and 250- μm -thick Nb layers, respectively.* For the crack to proceed through

*In the arrestor orientation, there is always some uncertainty over the precise value of K_0 depending upon whether the precrack is located in the intermetallic or Nb reinforcement layer. However, little variation was seen, presumably because precracks in the intermetallic readily propagate and "blunt" in the metal layer.

the composite, it must renucleate in the intermetallic phase beyond the ductile metal layer.^[30,33,40-43] This renucleation process has been determined to be a stress-based event^[30,44]

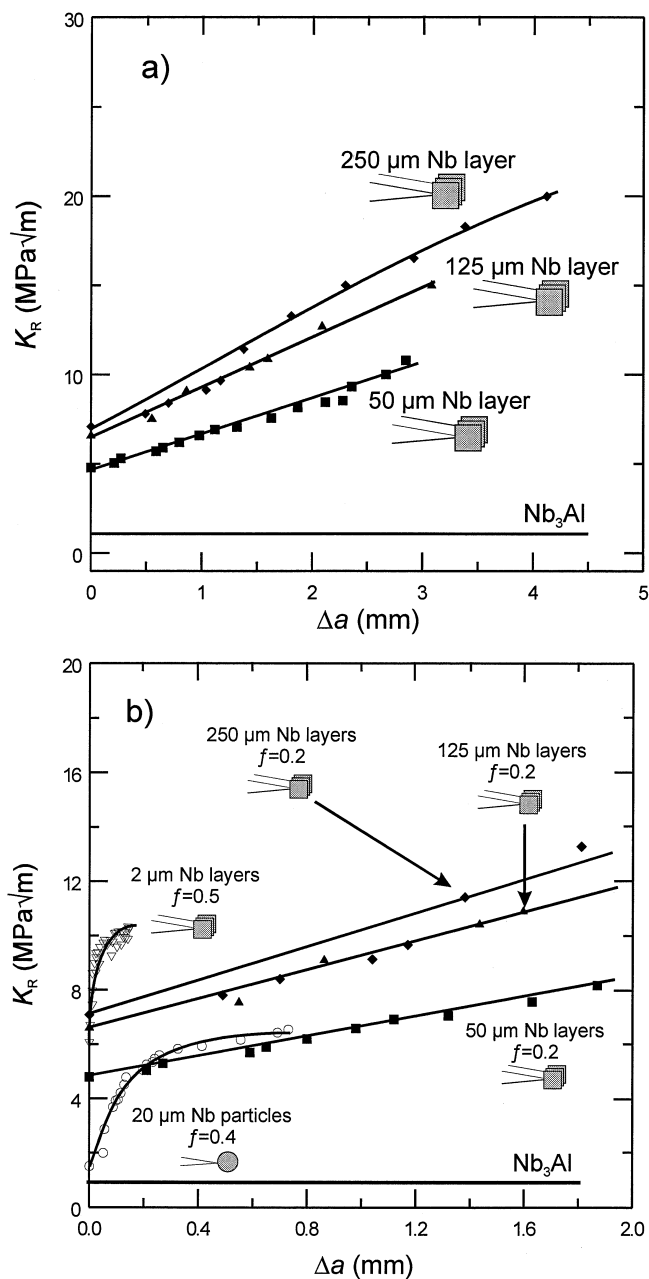
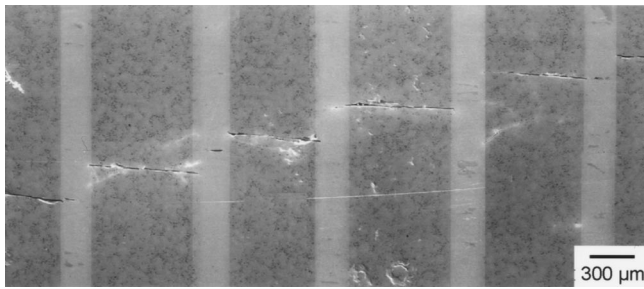


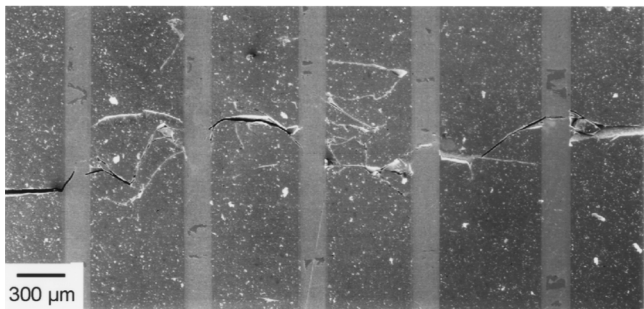
Fig. 4—(a) Comparison of the divider laminate R -curves showing improved toughness with increasing Nb layer thickness. (b) Expanded region of (a) showing the improved toughness obtained with the divider laminates of this study as compared to Nb/ Nb_3Al particulate and divider microlaminate composites.

similar to a Ritchie–Knott–Rice mechanism,^[45] where the local crack tip stress field must reach a critical value in order to fracture the brittle phase at some distance ahead of the crack tip. Consequently, the K_0 value for this laminate orientation is often significantly larger than the K_{Ic} of the matrix. Furthermore, in metal-reinforced ceramic laminates, it has been shown that K_0 scales directly with increasing reinforcement layer thickness.^[33,44,46,47] This is due to the larger far-field applied stresses necessary to drive the local fracture event because the brittle phase is farther from the crack tip.

A crack-growth toughness in excess of $\sim 18 \text{ MPa}\sqrt{\text{m}}$ was achieved for all arrestor layer thicknesses, and, for a given



(a)



(b)

Fig. 5—Micrographs of crack fronts showing (a) an example of crack tunneling in the fatigue crack growth region of a divider laminate and (b) an example of crack tunneling in the R -curve region of a divider laminate (~ 1.5 mm behind the crack tip). Note the non-coplanar cracks that form in the intermetallic in both cases. Crack growth direction is into the plane of the page.

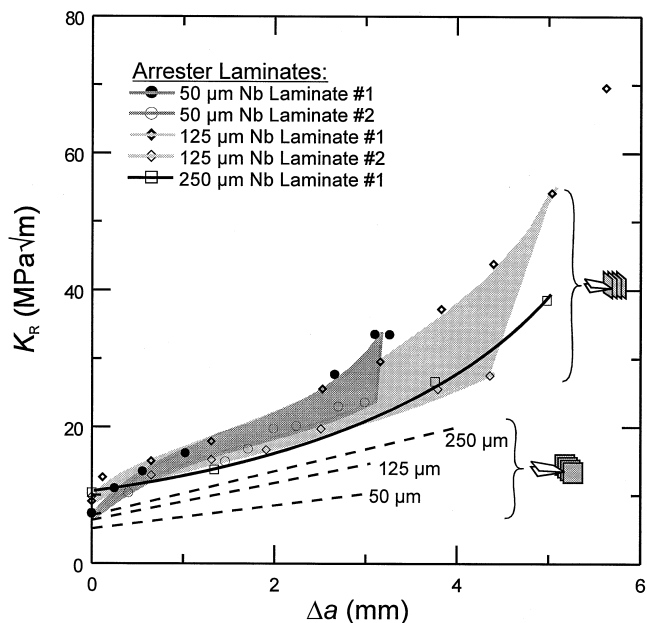


Fig. 6—Comparison of the R -curves measured for the arrester laminates to the divider laminates (dashed curves). The concave shape of the R -curves is a result of large scale bridging conditions.

layer thickness, this toughness was generally higher than that observed in the divider orientation. As described in Sections B and C, extensive crack bridging by unbroken Nb layers was again responsible for the order-of-magnitude

improvement in maximum toughness of the arrester laminates compared to unreinforced Nb_3Al .

3. Effect of laminate orientation

The difference in the fracture properties of the two orientations was relatively small (Figures 4 and 6). This was presumably due to the fact that both laminate orientations developed large bridging zones in the crack wake that were comparable in dimension with the length of the crack and remaining uncracked ligament; such LSB conditions invariably result in geometry-dependent behavior. Indeed, the “concave-up” shapes of the R -curves in Figure 6 strongly resemble those predicted by Cox and Lo^[48] for bridged cracks having frictional pull-out tractions behind the crack tip. The transition in shape from the typical R -curve, as shown by the particulate composite (Figure 4(b)), to the concave-up shapes of the arrester laminate (Figure 6) can be attributed to the transition from a fully developed equilibrium bridging zone to a non-fully developed bridging zone.

For crack-initiation toughness, the role of orientation was difficult to evaluate due to uncertainties associated with pre-cracking the divider specimens. However, for crack-growth toughness, steady-state bridging zone lengths in the arrester laminates (where $W \sim 9$ to 13 mm) were ~ 3 and 5.5 mm in the 50- and 125- μm Nb laminates, respectively; the 250- μm Nb laminate exhibited a fully bridged crack with no indication of failed ligaments over the entire range of crack extension. Similarly, for divider laminates (where $W = 33$ mm), fully bridged cracks with no evidence of bridging ligament failure were again observed; these zones were ~ 30 pct or more of the crack sizes and/or uncracked ligament sizes. For the test geometries used, LSB conditions were clearly prevalent.

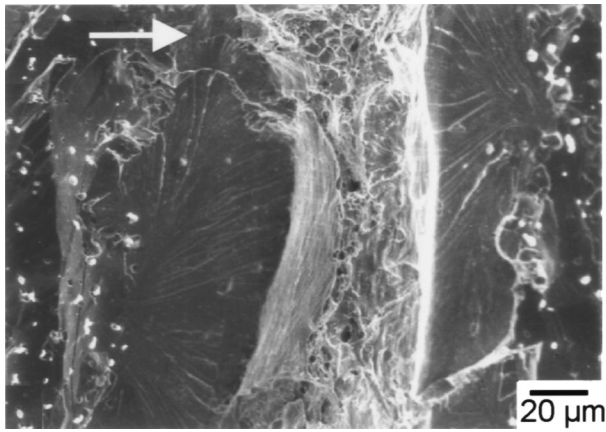
Despite the limitation of geometry-dependent R -curves under LSB conditions, which makes a comparison of specimen geometries difficult, information can be extracted from such R -curves in order to estimate the toughness in the (geometry-independent) SSB limit; such procedures are described in Section C.

B. Crack/Layer Interactions

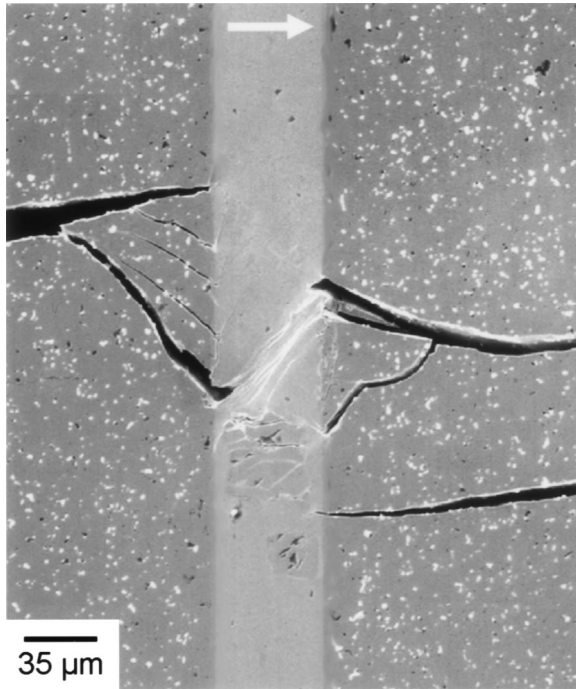
1. Arrester orientation

Metallography, combined with *in situ* telescopic observation, showed that the development of the R -curve was associated with the crack-reinforcement interactions, which involved crack arrest at the Nb layer, crack renucleation ahead of the layer, and repenetration of the crack into the reaction layer.^[40,41,42] The opposing direction of the river markings on the cleavage facets in the reaction zones on either side of the Nb layer indicated that the crack penetrated from both sides of the Nb layer (Figure 7(a)). With further increase in load, this process recurred as the crack advanced across several Nb layers leaving them intact, thereby forming large (>3 -mm) bridging zones in the crack wake. The Nb layers exhibited extensive shear band formation before final failure by ductile rupture (Figure 7(b)), when the bridging layer reached a critical displacement condition.

The intense shear banding in the Nb layers often resulted in the renucleation event being offset on one side of the layer compared to the other (Figure 7(b)). Such offset cracking acts to enhance the shielding effectiveness of the



(a)



(b)

Fig. 7—Micrographs showing evidence of a crack renucleation event in the arrester laminates. (a) Cleavage markings in the reaction layer indicate that the crack penetrated the Nb layer from both sides. (b) Non-coplanar cracking and near interfacial cracking result in shear band deformation in the bridging layer. The arrows indicate direction of crack growth.

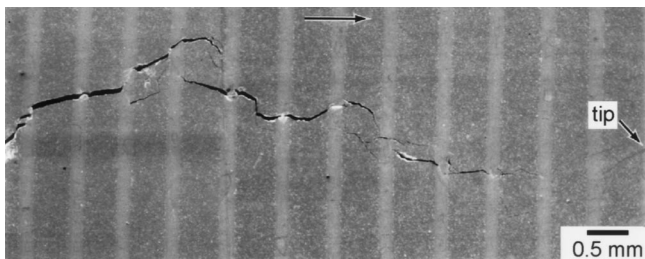


Fig. 8—Micrograph showing a single dominant crack despite local crack branching in the arrester orientation. The arrow indicates the direction of crack growth.

bridging layers because the work of rupture of the ductile bridge increases significantly when the metal layer shears

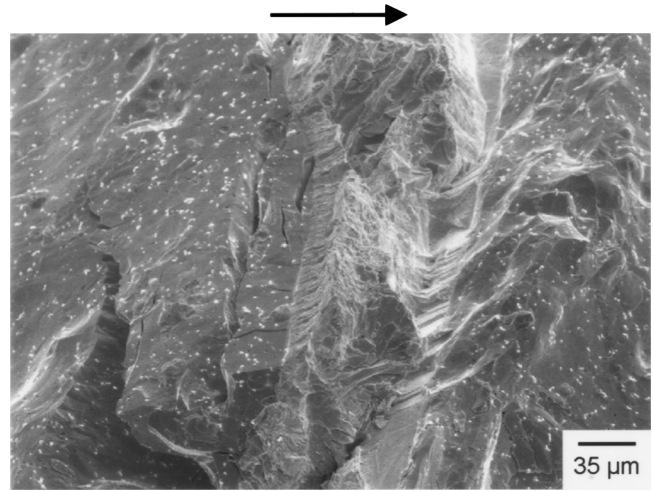


Fig. 9—Micrograph showing microvoid coalescence and plastic stretching observed in the Nb layer, where near interfacial cracking was present in the arrester laminate. The plastic stretching of the Nb layer can be seen by comparing the reduced cross section of the layer in the lower two-thirds of the micrograph to that of the upper portion. Also note the angled fracture surfaces of the Nb layer due to the failure from shear banding. The arrow indicates the crack growth direction. Micrograph was taken at a tilt angle of ~ 50 deg.

off at an angle.^[26] In addition, crack branching on one or both sides of the Nb layer commonly occurred in the matrix near the Nb/Nb₃Al interface, but not necessarily at the interface (Figure 7(b)). These branches then linked up to form a single dominant crack as the crack progressed across the specimen (Figure 8). Such near interfacial cracking acted to “debond” the Nb/Nb₃Al interface, which reduced the constraint and consequently promoted ductile failure in the Nb layer.^[8,26]* This behavior was confirmed by fractogra-

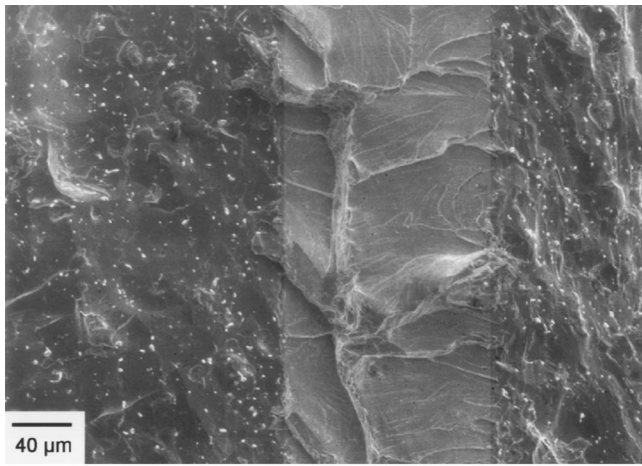
*The near-interfacial cracking and non-coplanar crack renucleation sites rarely exceeded one to two reinforcement layer thicknesses. As this is associated with reduced constraint in the layer,^[26] it can be speculated that the constraint of the reinforcing metal layer increases with decreasing layer thickness.

phy which revealed that, where bridging layers failed by microvoid coalescence, near interfacial cracking was typically involved and the ruptured bridging layers appeared to be angled (Figure 9).

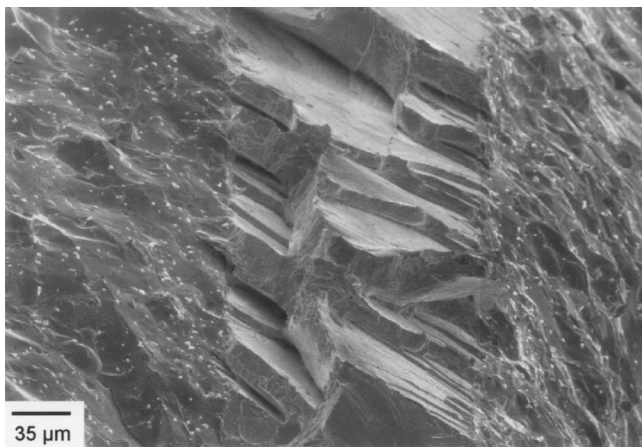
In contrast, in regions where near-interfacial secondary cracking was limited or absent, the increased constraint in the Nb layers led to failure by an apparent brittle cleavage-like mechanism (Figure 10(a)). However, high tilt-angle microscopy showed that the “cleavage” facets were a series of Nb ligaments which formed from parallel microcracks in the layer. The planar ligaments generally formed at an angle to the loading direction resulting in deformation by bending; final failure of the remaining uncracked regions then occurred by localized plasticity and microvoid coalescence (Figure 10(b)). Thus, in both modes of failure of the Nb layers (Figures 9 and 10), significant plastic energy dissipation contributed to an increased work of rupture of the layer, thereby toughening the laminate.

2. Divider orientation

Crack tunneling in the brittle intermetallic matrix was the predominant mechanism responsible for the bridging zones in the crack-divider orientation (Figure 5b). Although near



(a)

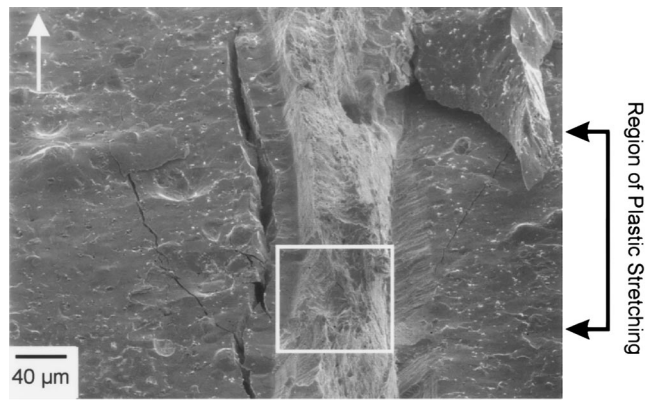


(b)

Fig. 10—Micrographs showing (a) apparent cleavage fracture of the Nb layer in regions where there was no near interfacial cracking (0 deg tilt angle), but (b) high tilt angle microscopy (tilt angle of ~60 deg) of pure region indicates that offset cracks form in the highly constrained Nb layer. This leads to intact ductile bridging ligaments, which dissipate plastic energy by microvoid coalescence and shear banding during failure. The arrow indicates the crack growth direction.

interfacial cracking was more frequent than in the arrester specimens, it was again observed that the cracks in the Nb₃Al layers propagated on a non-coplanar path (Figure 5b). This led to localized shear band deformation in the Nb bridging layers and angled fracture surfaces that revealed extensive microvoid coalescence in the fractured layers (Figure 11).

Metallographic sectioning during R-curve measurement indicated that a single crack grew stably for a several millimeters before appearing to arrest; however, upon further loading, an extensive microcrack zone (with dimensions of the order of 100 μm) developed ahead of the crack tip, making further definition of the crack length difficult (Figure 12). Measurements were typically halted at this point as a *K*-based “single dominant crack” approach becomes inappropriate. As shown in Figure 12, the microcracking zone envelops the main crack, extending both ahead of the original crack tip and deflecting completely around such that microcracks appear to be propagating back toward the



Magnified view of boxed region showing void coalescence

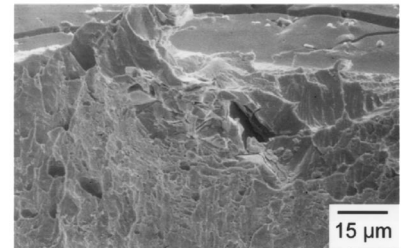


Fig. 11—Micrograph showing microvoid coalescence and plastic stretching observed in the Nb layer, where near interfacial cracking was present in the divider laminate. Plastic stretching of the Nb is indicated by the reduced cross section of the layer in the center of the micrograph. Also note the angled fracture surfaces of the Nb layer that result from shear band failure due to the non-coplanar cracking in the intermetallic. The arrow indicates the crack growth direction. Micrographs were taken at a tilt angle of ~50 deg.

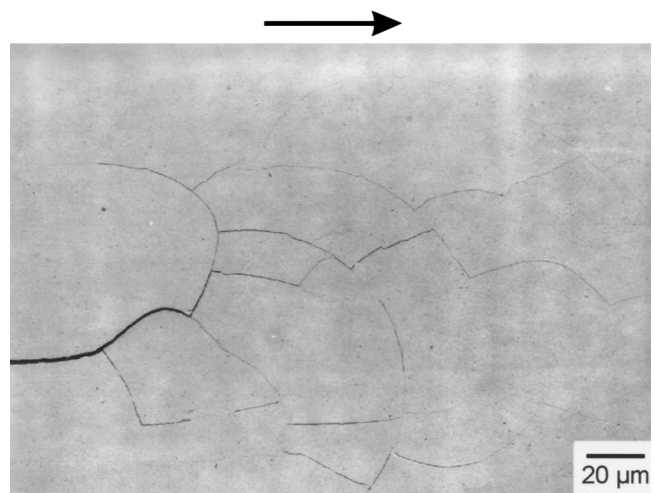


Fig. 12—Micrograph of the diffuse crack branching zone observed in the divider laminates after several millimeters of crack growth during R-curve testing. Notice the deflection of the crack back toward the load line of the DC(T) specimen. The arrow indicates the crack growth direction.

mouth of the specimen. Using metallographic sectioning (perpendicular to the crack and advancing from the notch tip toward the crack tip) in order to reveal the evolution of the microcrack zone, multiple cracking of the Nb₃Al could be observed as far back as ~1 to 2 mm behind the main

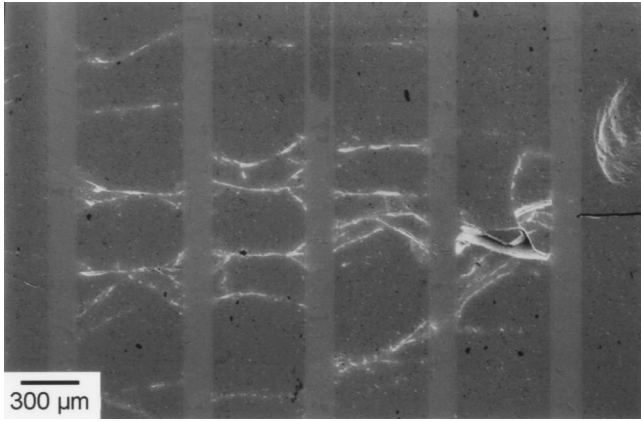


Fig. 13—Cross section of the crack front in the divider *R*-curve specimen taken at the approximate crack tip. In this case, a dominant crack tip becomes difficult to define. The crack growth direction is into the page.

crack tip, the extent of microcracking becoming progressively larger closer to the crack tip (Figure 13).*

*Whereas some of this damage clearly developed during *R*-curve testing, it is believed that it was exacerbated by the additional sustained loading period imposed to monitor the development of microcracking after the *R*-curve measurements had been halted.

C. Models for Toughening

From these experimental observations, it is apparent that the source of the *R*-curve (crack-growth) toughness in the Nb/Nb₃Al laminates is associated principally with the crack-tip shielding that results from the bridging of intact Nb layers in the wake of the crack. Quantitatively, the contribution to the toughness due to crack bridging can be obtained by calculating the reduction in the near-tip stress intensity, K_b , caused by the appropriate crack-surface traction stress distribution. The problem depends upon the given traction distribution, crack length, and specimen geometry; generalized solutions employ weight functions to calculate the stress intensity reduction caused by the shielding zone for any form of the traction function.^[48–53] The bridging contribution is formulated as

$$K_b = \int_L \sigma(x)h(a,x)dx \quad [4]$$

where $\sigma(x)$ is the traction as a function of distance x behind the crack tip, $h(a,x)$ is the weight function, and the integration limits are determined by the bridging zone length, L (x and L are measured from the load line or specimen edge (Figure 14)). If the shielding contribution is superposed with the intrinsic toughness of the composite, the measured toughness, $K_{c,app}$, for a given loading condition can be predicted by

$$K_{c,app} = K_0 + K_b \quad [5]$$

where K_0 is taken to be the crack-initiation toughness of the composite.

Computation of Eq. [4] requires knowledge of the traction function, $\sigma(x)$, which in turn depends on the stress-displacement behavior, $\sigma(u)$, of the bridging ligaments and the crack-opening profile, $u(x)$. These functions are gener-

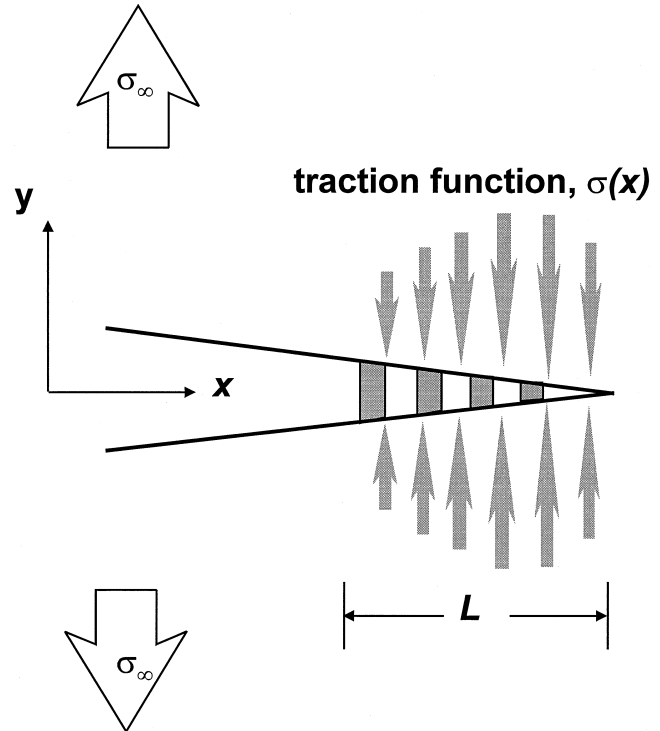


Fig. 14—Schematic representation of the model used to determine the shielding contribution provided by the Nb bridging ligaments in the crack wake. It is important to recognize that the integration length variable, x , is measured from the load line to the crack tip.

ally obtained by the direct measurement of the constrained stress-displacement behavior of the specific composite system* or of the crack-opening profile of the system under

*More recently, self-consistent numerical techniques have been developed to calculate these functions with only knowledge of the critical points of $\sigma(u)$ and $u(x)$,^[48] however, these methods have not received widespread use to date because of difficulties in obtaining stable solutions to the integral problems required by the technique and the intensive numerical analysis of the iterative solutions.

load.^[8,17,26,54]

A simplified approach to this problem is to assume that $\sigma(x)$ is a constant function and uniformly active over the bridging zone,^[18] the magnitude of the traction function is then equal to some characteristic flow parameter, σ_c , which effectively is the constrained flow stress of the metal reinforcement. Alternatively, it can be taken to be equivalent to the uniaxial yield or flow strength of the metal.^[18] The discreteness of the reinforcement is accounted for by multiplying by the volume fraction, f , of the reinforcement. With these assumptions, the function $\sigma(x)$ becomes $f\sigma_c$, and Eqs. [4] and [5] can be rewritten as

$$K_{c,app} = K_0 + f\sigma_c \int_L h(a,x)dx \quad [6]$$

Previous studies of Nb reinforcements in other intermetallic matrices, e.g., in MoSi₂^[55] and Nb₅Si₃,^[38] indicate that the constrained load/displacement curve for a constrained Nb layer rises rapidly to a relatively constant plateau with continuing displacement. Consequently, the assumption of a constant traction function for Nb-reinforced composites appears to be reasonable and, thus, is used in the following analysis of *R*-curve behavior.

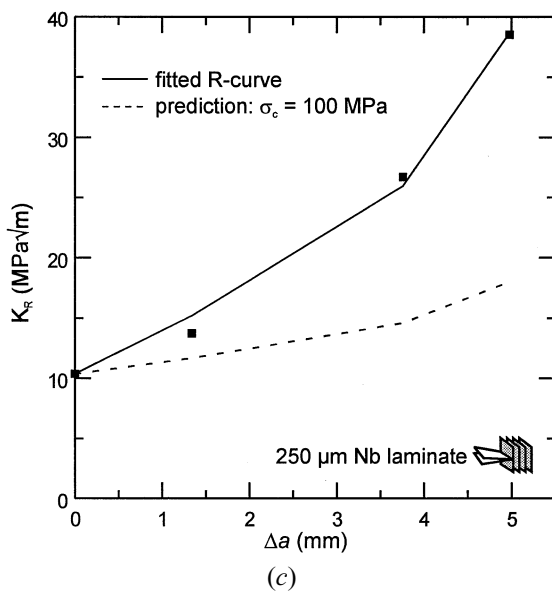
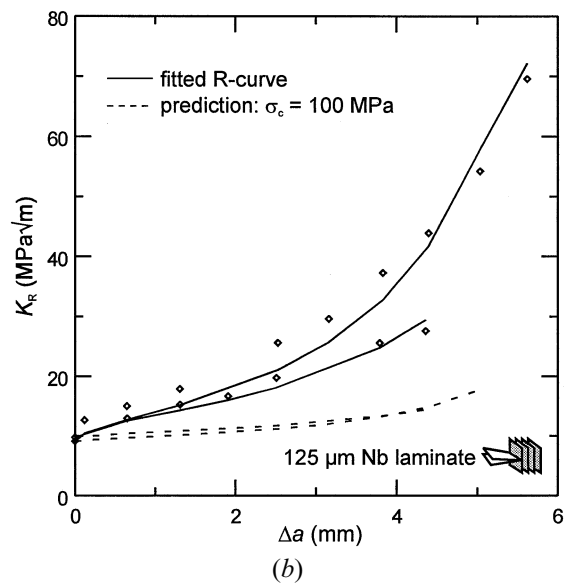
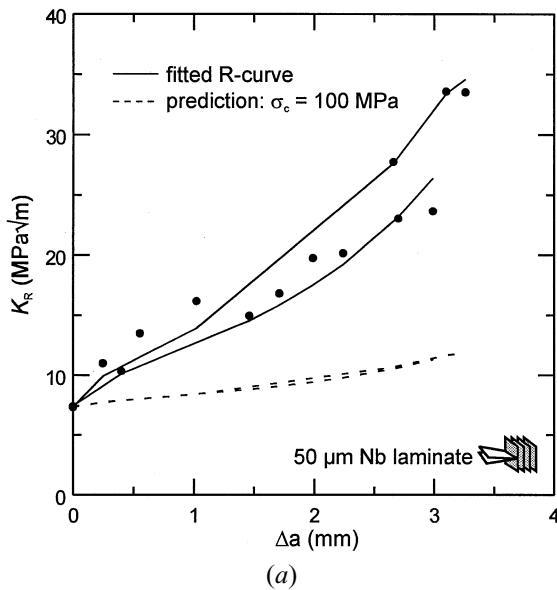


Fig. 15—Plots showing the R -curve predictions (using $\sigma_c = 100$ MPa) and the R -curve fits obtained using Eqs. [5] and [6] for (a) the 50 μm Nb arrester laminate, (b) the 125- μm Nb arrester laminate, and (c) the 250- μm Nb arrester laminate.

1. Arrester orientation

To obtain a prediction of the R -curve behavior for each laminate layer thickness, the weighting function for the bend geometry,^[49] given in the Appendix as Eq. [A1], was substituted into Eq. [6] and the combined equation integrated over the length of the bridging zone. The choice of the flow stress for the Nb layers was difficult to define, as the properties of Nb can vary significantly depending on the level of constraint imposed by the matrix and on the presence of impurities. Uniaxial yield strengths (for unconstrained conditions) ranging from 60 to 250 MPa have been reported,^[17,38,56,57] but a conservative value of 100 MPa is assumed here based on observations by Chung and Stoloff^[56] for large grain size ($>100\text{-}\mu\text{m}$) commercially pure Nb, similar to that used in the present study.

Corresponding R -curve predictions using a constant traction, $\sigma_c = 100$ MPa, in Eq. [6] are shown as dashed curves in Figure 15. It is clear that the unconstrained uniaxial yield strength of Nb severely underpredicts the measured toughness, suggesting that using a flow stress that properly re-

Table II. Calculated Constrained Flow Stress Values for Arrester Nb Reinforcement Layers

Nominal Nb Reinforcement Layer Thickness (μm)	Effective Constrained Flow Stress (MPa)	Average Effective Constrained Flow Stress (MPa)
50	600	540
	475	
125	560	490
	425	
250	370	370

flects the constraint imposed in the layers by the intermetallic matrix is necessary.

Alternatively, an effective constrained flow stress can be deduced using Eq. [6]. This involves iterating the calculations to obtain a value for σ_c that minimizes the residual defined by the square of the difference between the experimental data and the prediction. The results of these fits

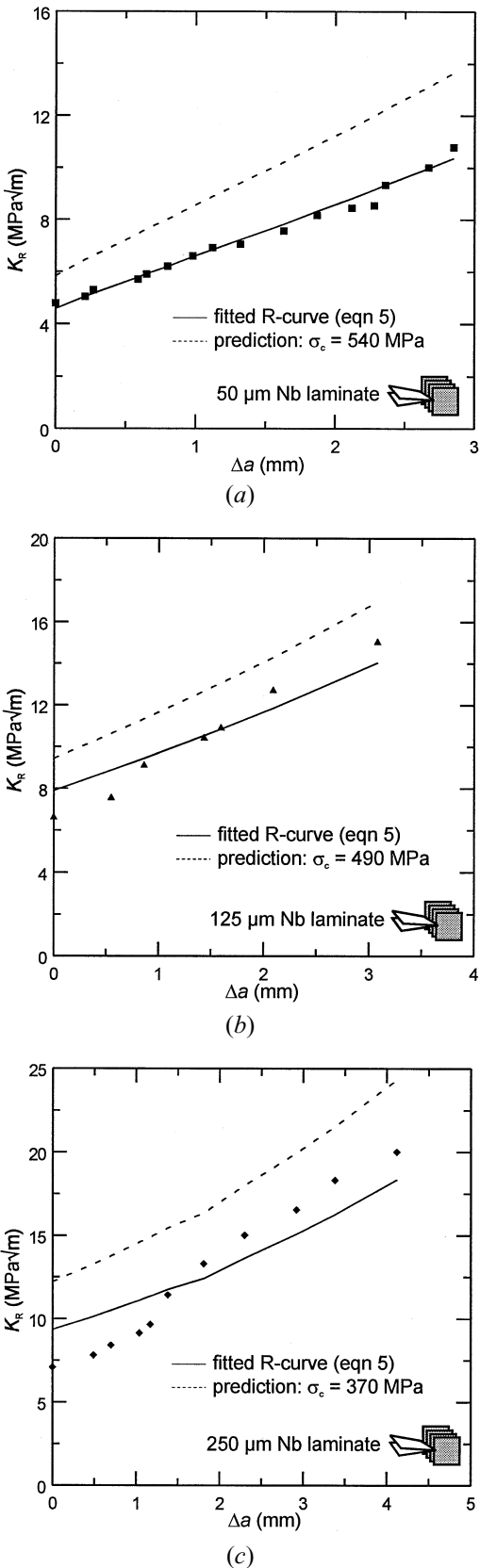


Fig. 16—Plots showing the R -curve predictions (using σ_c values calculated from the arrester analysis) and the R -curve fits obtained using Eqs. [5] and [6] for (a) the 50- μm Nb divider laminate, (b) the 125- μm Nb divider laminate, and (c) the 250- μm Nb divider laminate.

(solid curves in Figure 15) are given in Table II, which shows that the average constrained flow stress of the layers increases with decreasing layer thickness. This result supports the observation that the near interfacial cracking is more apparent with increasing Nb layer thickness, thus implying that constraint is reduced in the thicker layers. The higher constrained flow stresses are consistent with measured stresses as high as 7 times the uniaxial flow stress found in prior studies on constrained metal layers.^[8,17,26,55] Indeed, the 350 to 440 MPa values reported by Pickard and Ghosh^[55] for a 250- μm Nb layer in MoSi_2 compare well with the flow stress of ~ 370 MPa determined in the present study.

2. Divider orientation

Similar R -curve modeling was performed for the divider orientation using the appropriate weight function^[58] for the DC(T) sample, given in the Appendix as Eq. [A2]. However, somewhat different assumptions were used since the measured initiation toughness values are artificially high (because of the residual bridging zone left after precracking) and are thus not truly representative of the intrinsic toughness term in Eq. [6]. As previous studies on divider samples in a β -TiNb/ γ -TiAl system showed that the initiation toughness was approximately that of the matrix,^[28] a value equal to the intrinsic toughness of Nb_3Al , *i.e.*, $K_0 = 1 \text{ MPa}\sqrt{\text{m}}$, was assumed.

In addition, the constant traction σ_c values calculated from the arrester analysis were used for obtaining R -curve predictions in the divider orientation. For all layer thicknesses, these traction functions resulted in an overestimate of the monotonic crack-growth resistance, as shown by the dashed curves in Figure 16. This is not unprecedented, as analogous behavior was observed in the TiNb/TiAl laminates where the peak flow stress was slightly higher for the arrester than for the divider laminates (although the traction functions were not constant, as assumed here).^[28] As a result, the least-squares approach was used to calculate the appropriate magnitude of the constrained effective flow stress that gave the best fit to the experimental data for the divider orientation (solid curves in Figure 16); results are shown in Table III. The fits are again reasonably good for the measured R -curves. The constrained flow stresses show a similar trend to that seen in the arrester orientation, where the thinner layers are more constrained compared to thicker layers; however, the 50- and 125- μm Nb laminates showed the same constrained flow behavior. This could be due in part to the simplifying assumption of a constant traction function, and to the high sensitivity of constrained flow behavior on the interfacial properties between the metal and intermetallic phases.

The important feature of these predictions is that they support the assumption that the initiation toughness of the divider laminate was essentially that of the unreinforced matrix toughness. Furthermore, this K_0 value should be lower than that in the arrester orientation, because there is no need for any renucleation event to drive the crack into the intermetallic phase; however, the current experimental results do not show this trend clearly.

D. SSB Limit

Weight function methods can also be used to estimate the geometry-independent, steady-state toughness, K_{ss} , un-

Table III. Calculated Constrained Flow Stress Values for Divider Nb Reinforcement Layers

Nominal Reinforcement Layer Thickness (μm)	Effective Constrained Flow Stress (MPa)
50	400
125	400
250	275

der SSB conditions, provided that both the traction function and the bridging-zone length are known. As these features are known only for the 50- and 125- μm Nb arrester laminates, they are used here to estimate the SSB K_{ss} values. Assuming that the bridging-zone lengths are not a function of specimen size, K_{ss} can be calculated from Eqs. [6] and [A1] using a specimen width that is significantly larger than the bridging-zone size. Given bridging-zone sizes of 3 and 5.5 mm for the 50- and 125- μm Nb arrester laminates, respectively, it was found that specimen widths of ~ 80 and 180 mm would be required in order to obtain R -curves that reflected SSB conditions. The predictions, shown in Figure 17, indicate that R -curves under SSB conditions display a distinct plateau, with maximum (steady-state) toughnesses of 15.5 and 18.4 $\text{MPa}\sqrt{\text{m}}$ for the 50- and 125- μm Nb arrester laminates, respectively, indicating a clear toughness enhancement with the thicker reinforcement layers (Figure 17(c)).

Similar analyses could not be used for the other laminates, as no equilibrium bridging zones were found in the samples tested. As an alternative, the energy approach of Ashby and co-workers^[8] (Eq. [3]) can be used to estimate the SSB K_{ss} . To evaluate Eq. [3], we substitute the constrained flow stress value, calculated from the LSB analysis, for $\chi\sigma_0$ and correct the values of half-layer thickness r and volume fraction f of the Nb for the effect of the reaction-layer thickness to predict a SSB K_{ss} . Table IV shows the parameters and results of these calculations for the different layer thicknesses and laminate orientations.

The predictions of the SSB K_{ss} values of 17 and 22 $\text{MPa}\sqrt{\text{m}}$ obtained, respectively, for the 50- and 125- μm Nb arrester laminates using this simple physical model compare well with the corresponding predictions of the more rigorous weight function method of 15.5 and 18.4 $\text{MPa}\sqrt{\text{m}}$. This suggests that the use of the energy-based model is generally valid for these laminates, as maximum toughness values are reasonably consistent with measured values (Figures 4 and 6) for both laminate orientations, although it does appear to overpredict the maximum toughness. It would, therefore, be more conservative to treat the predictions of this model as an upper bound to the maximum toughness achievable for ductile-phase reinforced brittle matrix composites.

E. Role of Microstructure

The current work indicates that laminated composites provide optimal toughness properties compared to other reinforcement morphologies, as shown by K_{ss} toughnesses in Nb/Nb₃Al some 2 to 3 times higher than particulate-reinforced alloys. In particular, *coarser-scale* laminates appear to offer the best approach for achieving high toughness in ductile-phase reinforced brittle-matrix composites for struc-

tural applications. Properties, however, are dependent on laminate orientation and the reinforcing layer thickness.

1. Laminate orientation

Experimental and modeling studies show that the crack-arrester orientation provides the better initiation K_0 and growth K_{ss} toughnesses compared to the crack-divider composites. The higher K_0 values result from the renucleation event across the Nb reinforcing layer, which is necessary for crack propagation in the arrester laminates. Conversely, for the divider orientation, K_0 values approach that of the Nb₃Al matrix, consistent with earlier investigations of laminate fracture toughness behavior.^[28] With respect to crack-growth toughness, the difference between the two orientations is not large and is again likely to be related to crack renucleation. In the arrester orientation, renucleation events lead to complicated, meandering crack paths that result in complex deformation of the bridging Nb layers in the crack wake. This appears to promote enhanced crack-tip shielding compared to the relatively straight cracks in the divider orientation.

2. Reinforcement layer thickness

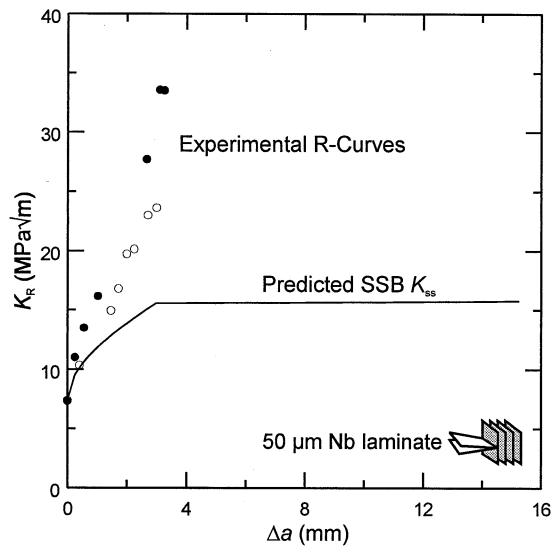
The thickness of the reinforcement layer (at a fixed reinforcement volume fraction) also has a significant influence on the toughness of the laminates. In the arrester orientation, the crack-initiation toughness is steadily increased with thicker Nb layers, as the renucleation event becomes more difficult. As the mechanism^[44] of crack renucleation can be associated with the local stress in the intermetallic exceeding a critical fracture stress to effect crack advance across the metal reinforcement, with increasing thickness of the ductile layer, the far-field stress must be increased in order for this criterion to be met. This results in a higher applied stress intensity and thus a higher measured K_0 with thicker ductile reinforcement layers. As renucleation is unnecessary in the divider orientation, K_0 values approach that of the intermetallic matrix, and there is little effect of reinforcing layer thickness on the crack-initiation toughness.

With respect to the crack-growth toughness, it is clear from both measurements and simple modeling that the thicker Nb reinforcing layers in the divider laminates result in a higher maximum toughness. This trend, however, is less obvious for the arrester laminates due to the influence of large-scale bridging. The origin of the improved toughness is most likely related to the larger bridging zones that develop with the thicker layers, although an additional factor may be associated with the lower constraint predicted by the weight function modeling in the thicker Nb bridging layers; such reduced constraint should allow for greater plastic deformation in the Nb bridging layers.

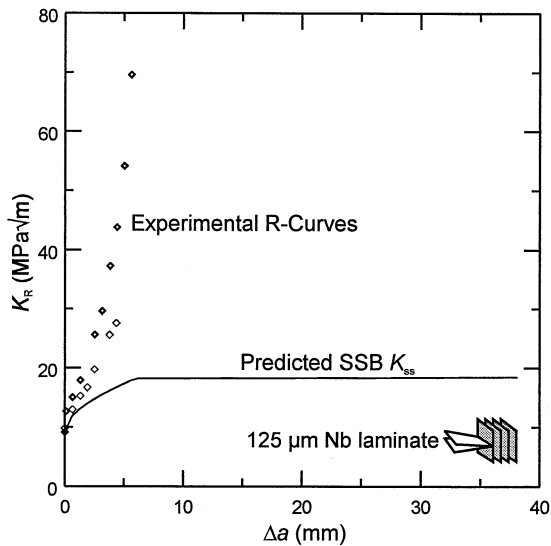
IV. CONCLUSIONS

Based on a study of the fracture toughness and resistance-curve behavior of the Nb-reinforced Nb₃Al laminates, the following conclusions can be made.

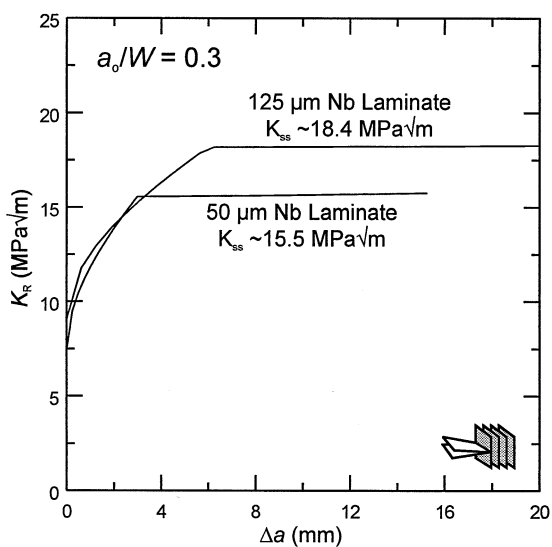
1. Marked improvements in the fracture toughness of brittle Nb₃Al intermetallics can be achieved using significantly lower volume fractions of ductile Nb reinforcements as coarse (50 to 250 μm) laminates, as compared to reinforcement by either Nb particulates or



(a)



(b)



(c)

Fig. 17—(a) Plot of the predicted SSB R -curve for the 50 μm Nb arrester laminate obtained from Eqs. [5] and [6] by assuming a $W \sim 80$ mm. (b) Plot of the predicted SSB R -curve for the 125- μm Nb arrester laminate obtained from Eqs. [5] and [6] by assuming a $W \sim 180$ mm. (c) A comparison plot of the two predicted SSB R curves showed that the trend of improved toughness with increasing Nb layer thickness was retained.

Table IV. SSB Toughness Predictions

Nominal Nb Thickness (μm)	f	E' (GPa)	$\chi\sigma_0$ (MPa)	r (μm)	K_0 ($\text{MPa}\sqrt{\text{m}}$)	Predicted K_{ss} ($\text{MPa}\sqrt{\text{m}}$)	Measured K_{ss}^* ($\text{MPa}\sqrt{\text{m}}$)
Arrester orientation							
50	0.16	143	540	20	7.3	~ 17	13 to 15
125	0.14	144	490	42.5	9	~ 22	15 to 20
250	0.17	143	370	109	10.4	~ 33	10 to 20
Divider orientation							
50	0.16	143	400	20	1	~ 13	11
125	0.15	143	400	47.5	1	~ 20	15
250	0.17	143	275	109	1	~ 27	20

*Estimated as the peak toughness on the R curve.

- by 2- μm -thick Nb microlaminate. Toughness improvements of ~ 2 to 3 times that of a particulate-reinforced Nb/Nb₃Al composite were readily achieved using 20 vol pct of the coarser Nb layers.
- The significant improvements in the toughness of the laminates were seen to be associated primarily with the

creation of large (millimeter-sized) bridging zones of intact Nb layers in the crack wake.

- The effect of laminate orientation on such measured toughness behavior was found to be relatively small, although the arrester laminates generally showed improved properties over the divider laminates. Higher

crack-initiation toughness K_0 values were observed for the arrester laminates, because the crack must renucleate across the Nb layer prior to further crack extension. However, residual bridging in the crack wake (from pre-cracking) prevented accurate measurement of K_0 values in the divider orientation, although R -curve modeling calculations do suggest that they are approximately equal to the matrix toughness.

- At a constant volume fraction of reinforcement of 20 vol pct Nb, the crack-initiation and maximum toughness properties progressively improved with increasing the reinforcement layer thickness, the effect being more apparent in the crack-divider orientation.
- Although unrealistically large samples would be required in the present laminates to avoid large-scale bridging conditions, simple modeling using both weight-function and energy-based methods is found to provide reasonable estimates for the geometry-independent, steady-state toughnesses under SSB conditions.

ACKNOWLEDGEMENTS

This work was funded by the United States Air Force Office of Scientific Research under the AASERT Program (Grant No. F49620-93-1-0441) as a supplement to Grant No. F49620-93-1-0107, with Dr. C.H. Ward as contract monitor. The authors thank Major Ward for his support and Drs. B.J. Dalgleish and L.C. DeJonghe for their help with the processing.

APPENDIX

Weight functions for the bend and compact tension geometries

The weight function for the single-edge notch (three- or four-point) bend SE(B) geometry with a half outer span-to-width ratio greater than unity can be written as follows:^[49]

$$h(a,x) = \sqrt{\frac{2}{\pi a}} \cdot \frac{1}{\sqrt{1 - \frac{x}{a}}} \cdot \left[1 + \sum_{(\nu,\mu)} \frac{A_{\nu\mu} \cdot \left(\frac{a}{W}\right)^\mu}{\left(1 - \frac{a}{W}\right)^{3/2}} \cdot \left(1 - \frac{x}{a}\right)^{\nu+1} \right] \quad [A1]$$

where the coefficients, $A_{\nu\mu}$, for the sum are given in Table AI.

Table AI. Coefficients of Fit Polynomial for SE(B) Beam Weight Function

ν	$\mu = 0$	1	2	3	4
0	0.4980	2.4463	0.0700	1.3187	-3.067
1	0.5416	-5.0806	24.3447	-32.7208	18.1214
2	-0.19277	2.55863	-12.6415	19.7630	-10.986

The corresponding weight function for the disk-shaped compact tension, DC(T), specimen is given as:^[58]

$$h(a,x) = \sqrt{\frac{2}{\pi a}} \cdot \frac{1}{\sqrt{1 - \frac{x}{a}} \cdot \left(1 - \frac{a}{W}\right)^{3/2}} \cdot \left[\left(1 - \frac{a}{W}\right)^{3/2} + \sum_{(\nu,\mu)} D_{\nu\mu} \cdot \left(1 - \frac{x}{a}\right)^{\mu+1} \cdot \left(\frac{a}{W}\right)^\nu \right] \quad [A2]$$

where the coefficients, $D_{\nu\mu}$, for the sum are given in Table AII.

Table AII. Coefficients of Fit Polynomial for DC(T) Weight Function

ν	$\mu = 0$	1	2	3	4
0	2.826	-5.865	0.8007	-0.2584	0.6856
1	-10.948	48.095	-3.839	1.280	-6.734
2	35.278	-143.789	6.684	-5.248	25.188
3	-41.438	196.012	-4.836	11.435	-40.140
4	15.191	-92.787	-0.7274	-7.328	22.047

REFERENCES

- G.F. Harrison and M.R. Winstone: in *Mechanical Behavior of Materials at High Temperature*, C. Moura Branco, R.O. Ritchie, and V. Sklenicka, eds., NATO ASI Series 3, Kluwer Academic Publishers, Sesimbra, Portugal, 1995, vol. 15, pp. 309-25.
- D.L. Anton and D.M. Shah: *High Temperature Ordered Intermetallic Alloys III*, C.T. Liu, A.I. Taub, N.S. Stoloff, and C.C. Koch, eds., Materials Research Society Symposia Proceedings, Materials Research Society, Pittsburgh, PA, 1989, vol. 133, pp. 361-71.
- D.L. Anton and D.M. Shah: *Intermetallic Matrix Composites*, D.L. Anton, P.L. Martin, D.B. Miracle, and R. McMeeking, eds., Materials Research Society Symposia Proceedings, Materials Research Society, Pittsburgh, PA, 1990, vol. 194, pp. 45-52.
- R.T. Fleischer: *High Temperature Ordered Intermetallic Alloys III*, C.T. Liu, A.I. Taub, N.S. Stoloff, and C.C. Koch, eds., Materials Research Society Symposia Proceedings, Materials Research Society, Pittsburgh, PA, 1989, vol. 133, pp. 305-10.
- D.M. Shah, D.L. Anton, and C.W. Musson: *Intermetallic Matrix Composites*, D.L. Anton, P.L. Martin, D.B. Miracle, and R. McMeeking, eds., Materials Research Society Symposia Proceedings, Materials Research Society, Pittsburgh, PA, 1990, vol. 194, pp. 333-40.
- A.G. Evans: *J. Am. Ceram. Soc.*, 1990, vol. 72 (2), pp. 187-206.
- R.O. Ritchie: *Mater. Sci. Eng. A*, 1988, vol. A103, pp. 15-28.
- M.F. Ashby, F.J. Blunt, and M. Bannister: *Acta Metall.*, 1989, vol. 37 (7), pp. 1847-57.
- A.G. Evans and R.M. McMeeking: *Acta Metall.*, 1986, vol. 34 (12), pp. 2435-41.
- B. Budiansky, J.C. Amazigo, and A.G. Evans: *J. Mech. Phys. Solids*, 1988, vol. 36 (2), pp. 167-87.
- V.V. Krstic, P.S. Nicholson, and R.G. Hoagland: *J. Am. Ceram. Soc.*, 1981, vol. 64 (9), pp. 499-504.
- L.S. Sigl, P.A. Mataga, B.J. Dalgleish, R.M. McMeeking, and A.G. Evans: *Acta Metall.*, 1988, vol. 36 (4), pp. 945-53.
- P.A. Mataga: *Acta Metall.*, 1989, vol. 37 (12), pp. 3349-59.
- K.T. Venkateswara Rao, W.O. Soboyejo, and R.O. Ritchie: *Metall. Trans. A*, 1992, vol. 23A, pp. 2249-57.
- L. Murugesu, K.T. Venkateswara Rao, and R.O. Ritchie: *Scripta Metall. Mater.*, 1993, vol. 29, pp. 1107-12.
- C.D. Bencher, A. Sakaida, K.T. Venkateswara Rao, and R.O. Ritchie: *Metall. Mater. Trans. A*, 1995, vol. 26A, pp. 2027-34.
- H.C. Cao, B.J. Dalgleish, H.E. Deve, C. Elliott, A.G. Evans, R. Mehrabian, and G.R. Odette: *Acta Metall.*, 1989, vol. 37 (11), pp. 2969-77.
- F. Zok and C.L. Hom: *Acta Metall. Mater.*, 1990, vol. 38 (10), pp. 1895-1904.
- B.D. Flinn, C.S. Lo, F.W. Zok, and A.G. Evans: *J. Am. Ceram. Soc.*, 1993, vol. 76 (2), pp. 369-75.
- D.E. Alman and N.S. Stoloff: *Metall. Mater. Trans. A*, 1995, vol. 26A, pp. 289-304.
- K. Badrinarayanan, A.L. McKelvey, K.T. Venkateswara Rao, and R.O. Ritchie: *Metall. Mater. Trans. A*, 1996, vol. 27A, pp. 3781-92.
- C.K. Elliott, G.R. Odette, G.E. Lucas, and J.W. Sheckard: *High-Temperature/High-Performance Composites*, F.D. Lemkey, A.G. Evans, S.G. Fishman, and J.R. Strife, eds., Materials Research Society Symposia Proceedings, Materials Research Society, Pittsburgh, PA, 1988, vol. 120, pp. 95-101.
- B.J. Dalgleish, K.P. Trumble, and A.G. Evans: *Acta Metall.*, 1989, vol. 37 (7), pp. 1923-31.

24. H.F. Dève, A.G. Evans, G.R. Odette, R. Mehrabian, M.L. Emiliani, and R.J. Hecht: *Acta Metall. Mater.*, 1990, vol. 38 (8), pp. 1491-1502.
25. T.C. Lu, A.G. Evans, R.J. Hecht, and R. Mehrabian: *Acta Metall. Mater.*, 1991, vol. 38 (8), pp. 1853-62.
26. M. Bannister and M.F. Ashby: *Acta Metall. Mater.*, 1991, vol. 39 (11), pp. 2575-82.
27. K.T. Venkateswara Rao, G.R. Odette, and R.O. Ritchie: *Acta Metall. Mater.*, 1992, vol. 40 (2), pp. 353-61.
28. G.R. Odette, B.L. Chao, J.W. Sheckhard, and G.E. Lucas: *Acta Metall. Mater.*, 1992, vol. 40 (9), pp. 2381-89.
29. F.E. Heredia, M.Y. He, G.E. Lucas, A.G. Evans, H.E. Dève, and D. Konitzer: *Acta Metall. Mater.*, 1993, vol. 41 (2), pp. 505-11.
30. M.Y. He, F.E. Heredia, D.J. Wissuchek, M.C. Shaw, and A.G. Evans: *Acta Metall. Mater.*, 1993, vol. 41 (4), pp. 1223-28.
31. W.O. Soboyejo, K.T. Venkateswara Rao, S.M.L. Sastry, and R.O. Ritchie: *Metall. Trans. A*, 1993, vol. 24A, pp. 585-600.
32. W.O. Soboyejo and S.M.L. Sastry: *Mater. Sci. Eng.*, 1993, vol. A171, pp. 95-104.
33. M.C. Shaw, D.B. Marshall, M.S. Dadkhah, and A.G. Evans: *Acta Metall. Mater.*, 1993, vol. 41 (11), pp. 3311-22.
34. K.T. Venkateswara Rao, G.R. Odette, and R.O. Ritchie: *Acta Metall. Mater.*, 1994, vol. 42 (3), pp. 893-911.
35. H.C. Cao, J.P. Löfvander, A.G. Evans, R.G. Rowe, and D.W. Skelly: *Mater. Sci. Eng.*, 1994, vol. A185, pp. 87-95.
36. R.G. Rowe, D.W. Skelly, M. Larsen, J. Heathcote, G. Lucas, and G.R. Odette: *High Temperature Silicides and Refractory Alloys*, C.L. Bryant et al., eds., Materials Research Society Symposia Proceedings, Materials Research Society, Pittsburgh, PA, 1994, vol. 322, pp. 461-72.
37. Q. Ma, M.C. Shaw, M.Y. He, B.J. Dalgleish, D.R. Clarke, and A.G. Evans: *Acta Metall. Mater.*, 1995, vol. 43 (6), pp. 2137-42.
38. J. Kajuch, J. Short, and J.J. Lewandowski: *Acta Metall. Mater.*, 1995, vol. 43 (5), pp. 1955-67.
39. J. Heathcote, G.R. Odette, and G.E. Lucas: *Acta Mater.*, 1996, vol. 44 (11), pp. 4289-99.
40. D.R. Bloyer, K.T. Venkateswara Rao, and R.O. Ritchie: *Mater. Sci. Eng. A*, 1996, vol. A216, pp. 80-90.
41. D.R. Bloyer, K.T. Venkateswara Rao, and R.O. Ritchie: *Johannes Weertman Symp.*, R.J. Arsenault, D. Cole, T. Gross, G. Kostorz, P. Liaw, S. Parameswaran, and H. Sizek, eds., TMS, Warrendale, PA, 1996, pp. 261-66.
42. D.R. Bloyer, K.T. Venkateswara Rao, and R.O. Ritchie: *Layered Materials for Structural Applications*, J.J. Lewandowski, C.H. Ward, M.R. Jackson, and W.H. Hunt, Jr., eds., Materials Research Society Symposia Proceedings, Materials Research Society, Pittsburgh, PA, 1996, vol. 434, pp. 243-48.
43. D.R. Bloyer, K.T. Venkateswara Rao, and R.O. Ritchie: *Mater. Sci. Eng. A*, 1997, vols. A239-A240, pp. 393-98.
44. H.C. Cao and A.G. Evans: *Acta Metall. Mater.*, 1991, vol. 39 (12), pp. 2997-3005.
45. R.O. Ritchie, J.F. Knott, and J.R. Rice: *J. Mech. Phys. Sol.*, 1973, vol. 21 (6), pp. 395-410.
46. Y. Huang, H.W. Zhang, and F. Wu: *Int. J. Solids Struct.*, 1994, vol. 31 (20), pp. 2753-68.
47. Y. Huang and H.W. Zhang: *Acta Metall. Mater.*, 1995, vol. 43 (4), pp. 1523-30.
48. B.N. Cox and C.S. Lo: *Acta Metall. Mater.*, 1992, vol. 40 (1), pp. 69-80.
49. T. Fett and D. Munz: *Stress Intensity Factors and Weight Functions for One-Dimensional Cracks*, Institut für Materialforschung: Kernforschungszentrum, Karlsruhe, Germany, 1994.
50. B.N. Cox and D.B. Marshall: *Acta Metall. Mater.*, 1991, vol. 39 (4), pp. 579-89.
51. F. Erdogan and P.F. Joseph: *J. Am. Ceram. Soc.*, 1989, vol. 72 (2), pp. 262-70.
52. R.M.L. Foote, Y.W. Mai, and B. Cotterell: *J. Mech. Phys. Sol.*, 1986, vol. 34 (6), pp. 593-607.
53. A.C. Kaya and F. Erdogan: *Int. J. Fract.*, 1980, vol. 16 (2), pp. 171-90.
54. M. Bannister, H. Shercliff, G. Bao, F. Zok, and M.F. Ashby: *Acta Metall. Mater.*, 1992, vol. 40 (7), pp. 1531-37.
55. S.M. Pickard and A.K. Ghosh: *Metall. Mater. Trans. A*, 1996, vol. 27A, pp. 909-21.
56. D.W. Chung and N.S. Stoloff: *Metall. Trans. A*, 1978, vol. 9A, pp. 1387-99.
57. J.M. Meininger and J.C. Gibeling: *Metall. Trans. A*, 1992, vol. 23A, pp. 3077-84.
58. T. Fett: *Int. J. Fract.*, 1993, vol. 63, pp. R81-R85.